

DISCOVERY OF SIX OPTICAL PHASE CURVES WITH *K2*

PRAJWAL NIRLA^{1,2}, SETH REDFIELD², JULIEN DE WIT¹, FEI DAI^{3,4}, ISMAEL MIRELES², DILOVAN SERINDAG⁵, AVI SHPORER⁶

¹Department of Earth, Atmospheric and Planetary Sciences, MIT, 77 Massachusetts Avenue, Cambridge, MA 02139, USA; Corresponding author: pniraula@mit.edu

²Astronomy Department and Van Vleck Observatory, Wesleyan University, Middletown, CT 06459, USA

³Department of Physics and Kavli Institute for Astrophysics and Space Research, Massachusetts Institute of Technology, Cambridge, MA 02139, USA

⁴Department of Astrophysical Sciences, Peyton Hall, 4 Ivy Lane, Princeton, NJ 08540 USA

⁵Leiden Observatory, Leiden University, P.O. Box 9513, 2300 RA Leiden, The Netherlands

⁶Department of Physics and Kavli Institute for Astrophysics and Space Research, Massachusetts Institute of Technology, Cambridge, MA 02139, USA

ABSTRACT

We have systematically searched for the phase curves among the planets discovered by *K2*. Using the reported planetary parameters, we screen out the best potential candidates, and examine their light curves in detail. For our work, we consider light curves from two different detrending pipelines - EVEREST and K2SFF. In order to remove stellar variability and systematics, we test three different filtering techniques: spline, phasma (median-filtering) and Butterworth (harmonics filtering). We find the Butterworth as the most robust performer in our injection-retrieval test. We have identified 6 previously unreported phase curves among the planets observed with *K2*: K2-31b, HATS-9b, HATS-11b, K2-107b, K2-131b, and K2-106b. The first four of these are hot Jupiters that have estimated photometric masses consistent with their RV-based masses within 2σ , 1σ , 1σ , and 3σ respectively, while the last two are ultra-short period super-Earths with phase curves dominated by reflective and thermal components. We also detect a secondary eclipse in HATS-11b. We thus deem it to be possible to validate the planetary nature of selected *K2* targets using photometry alone without RV, and suggest similar vetting could be used for the ongoing *TESS* mission.

Keywords: planetary systems: K2-31b, HATS-9b, HATS-12b, K2-107b, K2-131b, K2-106b and HATS-11b— technique: photometric

1. INTRODUCTION

Phase curve analysis has established itself as an important tool in characterizing exoplanets. It is commonly used for close-in massive planets, opening up a window to independently characterize the planetary parameters such as eccentricity, geometric albedo, longitudinal temperature distribution, cloud coverage as well as planetary mass (Shporer 2017; Parmentier & Crossfield 2018). While infrared windows are often ideal for observing the thermal phase curve of planets as planetary emission often peak in such bandpass (Harrington et al. 2006; Knutson et al. 2007; Adams & Laughlin 2018), the limited number of space based infrared facilities has been the primary bottleneck for such studies. This is where space-based photometric missions such as Convection, Rotation, and planetary Transits (*CoRoT*; Baglin et al. 2002), and *Kepler* (Borucki et al. 2010) have come in to play a crucial role through optical phase curves.

While leading in the discoveries of the exoplanets, these missions have also significantly increased the number of phase curve detections. For instance with *Kepler*, photometric time series were obtained for thousands of targets with unprecedented precision (e.g. 29.0 ppm Combined Differential Photometric Precision for Kp = 11.5 to 12 mag stars in the long cadence mode (Gilliland et al. 2011)). This has already led to the discovery of robust phase curves for more than 20 transiting *Kepler* planets (Esteves et al. 2015; Angerhausen et al. 2015). Additionally, the precise photometry has been used for exoplanet validation by providing an RV-independent estimate of planetary mass (Esteves et al. 2013; Faigler et al. 2013), as well as for the discovery of non-transiting systems (Faigler et al. 2012; Millholland & Laughlin 2017).

Despite operating only on two reaction wheels, the revamped *K2* mission is able to achieve photometric precision on par with the original *Kepler* mission. This has

been possible not only due to ingenious mission redesign (Howell et al. 2014) but also because of a host of tools that have been developed in response to the unique data challenges caused primarily by, but not limited to, the telescope drift (Vanderburg & Johnson 2014; Luger et al. 2016). Despite the short observation baseline of *K2* (around 80 days compared to almost four years for the primary *Kepler* mission), the observation of numerous brighter targets ($V \sim 10$ mag) with high precision does translate into good opportunities for detecting phase curves.

Yet, there are unique challenges in studying phase curves with a ‘short’ observation baseline. Not only does the shorter length of observation make it particularly difficult when it comes to disentangling the phase curve from quasi-periodic signals such as those arising from spot modulation, but non-periodic effects such as thermal settling or edge effects will disproportionately distort the final obtained signal. In the case of *K2*, the required aggressive post processing of the data to correct the systematics can also affect the astrophysical signal under consideration. Not to mention, there are gaps in our understanding of the physics behind phase curves. Intriguing questions surrounding the existence and the cause of the third harmonics observed in systems such as HAT-P-7b and Kepler-13Ab still eludes a clear explanation (Shporer et al. 2014; Esteves et al. 2015; Cowan et al. 2017). A handful of the optical phase curves have been observed with significant asymmetries, which have been attributed to scattering due to inhomogeneous clouds (Demory et al. 2013; Shporer & Hu 2015). Meanwhile, the temporal aspect of the optical phase curve has also recently noticed (Armstrong et al. 2016) which comes with the prescription for the climatic variability in planets, thereby undermining the classical picture of a consistent signal present throughout the time series. Similarly, given the small signal amplitude, correlated noise as well as dilution can dramatically affect the inferred conclusions we derive from the phase curves (see discussions surrounding Kepler-91b in Esteves et al. 2013; Lillo-Box et al. 2014). This all points to the complex world of planetary atmospheres hidden under the simple phase curve models, robust characterization of which would require more precise data.

Despite these challenges, there are already three reported planetary phase curves in *K2* data: Qatar 2b (Dai et al. 2017b), K2-141b (Malavolta et al. 2018), and WASP-104b (Močnik et al. 2018). Hot Jupiters like Qatar-2b and WASP-104b have light curves exhibiting ellipsoidal variation and Doppler boosting consistent with their radial velocity (RV) based masses. On the other hand, K2-141 b, an ultra short period super-Earth, has a measurable phase curve dominated by reflective and thermal components. Thus as more than 350 plan-

ets have been discovered by *K2*, we have undertaken a project to systematically search for phase curves among the *K2* light curves.

Through this work, we have detected phase curves yielding photometric masses within 3σ of the known RV masses for four hot Jupiters, and also have detected reflective as well as thermal components dominated phase curves for two ultra-short period super-Earths. Our work has been made possible by the availability of high quality data products for *K2* coupled with the use of a better filtering algorithm tested using signal injection and retrievals studies. The process we outline here in essence can be used to validate the planetary nature for certain candidates using *K2* photometry and stellar parameters alone.

2. POTENTIAL CANDIDATES

For this study, we have only considered the confirmed exoplanets. Our search included 382 exoplanets which were observed by *K2*, all of which were catalogued in NASA Exoplanet Archive¹ as of December 18, 2018 with the *K2* flag. While the *K2* mission itself has come to an end, the data from the mission is still being processed and many candidates are still being followed up, which will elevate the discovery numbers. The procedure we outline here can be used for any future exoplanets discovered by *K2* as well as from any other photometric surveys such as Transiting Exoplanet Search Survey (*TESS*; Ricker et al. 2015). Since the possibility of the detection of phase curves primarily boils down to the precision of the light curve, we filter out the suitable candidates by estimating the magnitude of the combined signal against the obtainable precision of the light curve.

We use the parameters recorded in the database to estimate the equivalent amplitude of the phase curve signal. When some of the values were missing, estimates were made based on other available parameters of the planet. Using the combined amplitude of all four different effects i.e. reflective, thermal, ellipsoidal and doppler components, we calculate the expected signal to noise ratio using an estimator for the precision of the light curve as below:

$$\begin{aligned} \text{SNR} &= \frac{((A_{Ref} + A_{Th})^2 + A_{Ell}^2 + A_{Dop}^2)^{\frac{1}{2}} \cdot N^{\frac{1}{2}}}{\sqrt{2}\sigma} \\ &= \frac{A_{Eqv} \cdot N^{\frac{1}{2}}}{\sqrt{2}\sigma} \end{aligned} \quad (1)$$

where N is the number of observed photometric points set to 3500 (roughly 30 minutes bin over 80 days observation period), and σ is the precision expected to be deter-

¹ <https://exoplanetarchive.ipac.caltech.edu>

mined by the brightness of the target in *Kepler* bandpass using pre-flight estimates. The equivalent amplitude is considered to be the amplitude of the sinusoidal signal which has power equivalent to the combined elements of the phase curve:

$$A_{Eqv} = ((A_{Ref} + A_{Th})^2 + A_{Ell}^2 + A_{Dop}^2)^{\frac{1}{2}} \quad (2)$$

To estimate the reflective component (A_{Ref}), we assume the geometric albedo (A_g) of 0.4 and evaluate the reflective component (A_{Ref}) as follows:

$$A_{Ref} = A_g \left(\frac{R_p/R_*}{a/R_*} \right)^2, \quad (3)$$

where R_p/R_* is the scaled radius of the planet, and a/R_* is the scaled semi-major axis. Similarly, the thermal

variation (A_{Th}) is calculated as:

$$A_{Th} = \left(\frac{R_p}{R_*} \right)^2 \frac{\int B(T_{Day})R(\lambda)d\lambda}{\int B(T_*)R(\lambda)d\lambda}, \quad (4)$$

where $B(T)$ is the Planck's black body radiation law corresponding to temperature T , $R(\lambda)$ is the response function of *Kepler/K2*, and T_{Day} is the day-side temperature of the planet, which is estimated as following:

$$T_{Day} = T_{eff} \sqrt{\frac{1}{a/R_*} [f(1 - A_B)]^{\frac{1}{4}}}, \quad (5)$$

where T_{eff} is the effective temperature of the host star, A_B is the Bond albedo set at 0.6 following a Lambertian sphere relation ($A_B = \frac{3}{2}A_g$), and f is a proxy variable for re-circulation set at 2/3 corresponding to the case where only the day-side is re-radiating (López-Morales & Seager 2007).

Table 1. Estimated amplitude of various phase curve components in ppm of *K2* targets sorted by expected SNR

Identifier	EPIC ID	Kp (Mag)	Period (Days)	R_p/R_*	A_{Ref}	A_{Th}	A_{Ell}	A_{Dop}	SNR
K2-31b	204129699	10.6	1.258	0.135	199.2	1.4	11.9	4.7	228.9
WASP-85 Ab	201862715	10.3	2.656	0.163	144.5	0.80	2.2	2.1	200.2
K2-237b	229426032	11.5	2.181	0.118	184.1	5.8	8.8	2.4	132.9
HAT-P-56b	202126852	10.9	2.791	0.105	109.5	3.0	7.0	2.8	109.3
WASP-104b^a	248662696	11.6	1.755	0.121	138.4	0.9	5.8	2.7	91.9
QATAR-2b^b	21275629	13.0	1.337	0.162	247.6	0.4	18.5	8.3	65.1
K2-183b	211562654	12.8	0.469	0.027	152.8	50.6	1.9	0.0	63.2
WASP-75b	206154641	11.8	2.484	0.103	103.8	1.7	4.2	1.7	61.8
WASP-118b	220303276	10.9	4.046	0.082	59.9	1.2	1.5	0.6	58.1
K2-260 b	246911830	12.5	2.627	0.097	135.3	5.3	7.9	1.9	52.9
K2-34b	212110888	11.4	2.996	0.088	65.5	0.9	6.3	2.5	47.3
K2-141b^c	246393474	10.6	0.280	0.020	31.6	2.4	2.8	0.1	38.6
HATS-9b	217671466	13.1	1.915	0.083	145.5	3.7	13.6	1.8	37.0
WASP-28b	60017806	11.9	3.407	0.116	69.7	0.4	1.5	1.4	36.9
K2-266b	248435473	11.4	0.659	0.043	46.2	0.4	1.1	0.2	34.2
WASP-55b	212300977	11.7	4.466	0.125	52.4	0.1	0.5	0.8	32.2
K2-107b	216468514	12.8	3.314	0.083	83.3	1.8	4.1	1.1	26.6
WASP-47b	206103150	11.8	4.161	0.102	44.1	0.1	1.6	1.8	25.9
HATS-12b	218131080	12.7	3.143	0.063	73.2	4.2	17.8	2.8	25.6
WASP-107b	228724232	11.2	5.721	0.145	25.5	0.0	0.0	0.3	20.4
K2-29b	211089792	12.9	3.259	0.142	72.9	0.7	0.9	1.4	20.4
HD 3167b	220383386	9.0	0.957	0.017	7.3	1.4	0.4	0.0	19.3
K2-39b	206247743	10.6	4.605	0.019	12.7	0.4	5.0	0.2	16.4
HATS-11b	216414930	13.7	3.619	0.107	97.1	1.2	3.1	1.3	15.5
K2-267b	246851721	11.3	6.180	0.0681	19.3	0.1	0.1	0.1	15.3
WASP-157b	212697709	12.2	3.952	0.094	33.8	0.1	0.5	0.8	15.2

Table 1 continued

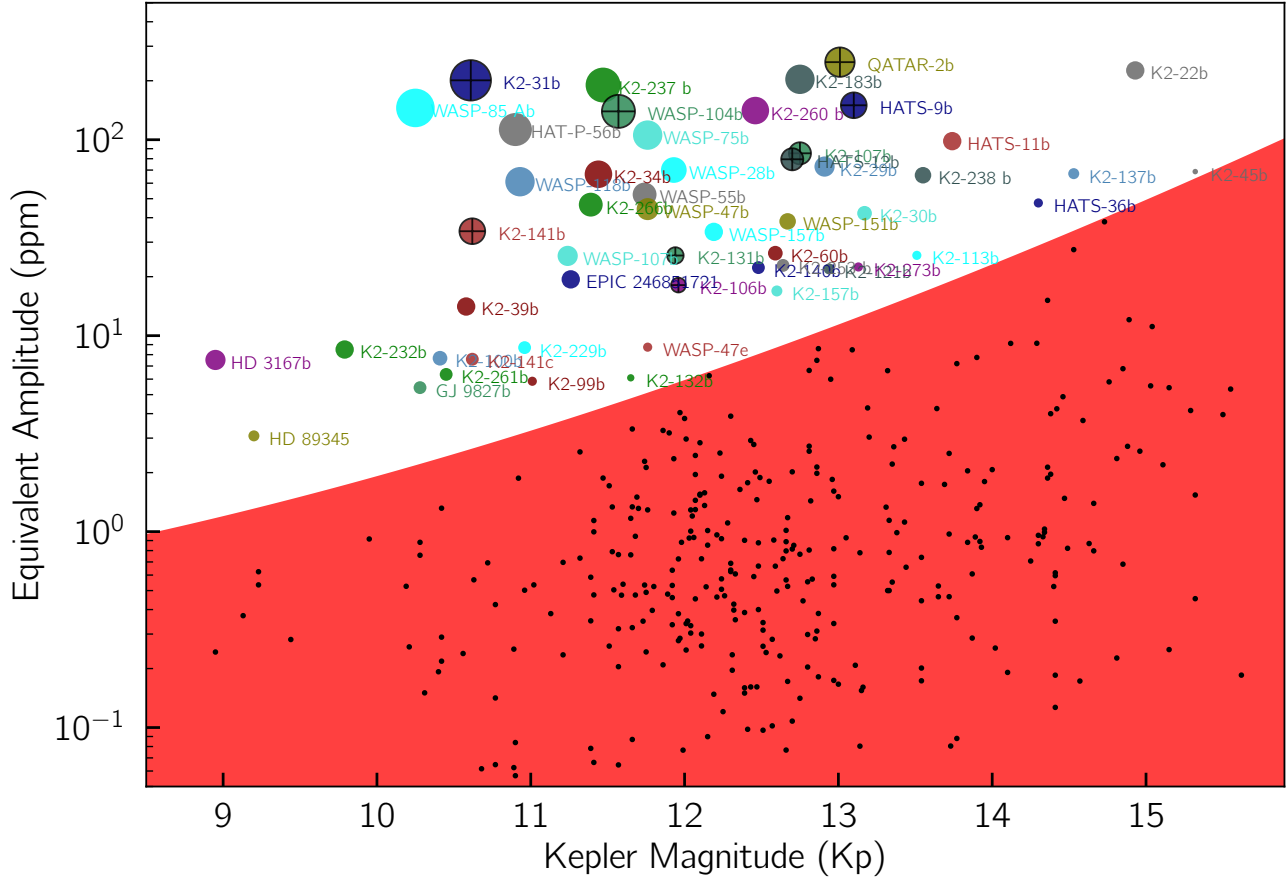


Figure 1. Expected signal amplitude (A_{eqv}) versus the *Kepler* magnitude for the *K2* detected planets. The red region contains the planet for which SNR detection is expected to be less than 3σ . For potentially detectable planets (i.e. $SNR > 3\sigma$), the size of the circle log-linearly increases with the expected SNR. The planets are given different colors in order to improve the readability of the graph. Out of 382 planets, 52 could have detectable phase signal above 3σ level and are listed in [Table 1](#). Among these, 9 planets have detected phase curves, all of which are marked in with black cross-hairs. Note the division between the two section roughly follows the pre-flight precision estimates as shown in [Figure 2](#), which overpredicts for the high magnitude star, and underpredicts for the low magnitude star.

Table 1 (*continued*)

Identifier	EPIC ID	Kp (Mag)	Period (Days)	R_p/R_*	A_{Ref}	A_{Th}	A_{EU}	A_{Dop}	SNR
K2-232b	247098361	9.79	11.168	0.020	8.5	0.0	0.1	0.4	14.8
K2-22b	201637175	14.9	0.381	0.075	205.8	1.8	87.7	9.0	14.5
K2-131b	228732031	11.9	0.369	0.020	23.5	2.1	1.8	0.1	13.5
WASP-151b	246441449	12.7	4.533	0.101	38.2	0.1	0.3	0.4	12.6
K2-238 b	246067459	13.6	3.205	0.080	65.1	0.6	3.8	1.3	11.8
K2-30b	210957318	13.2	4.100	0.127	42.1	0.0	0.5	1.0	9.9
K2-100b	211990866	10.4	1.674	0.027	7.5	0.1	0.1	0.0	9.7
K2-106b	220674823	12.0	0.571	0.017	16.3	1.7	2.0	0.1	9.4
K2-60b	206038483	12.6	3.003	0.063	26.2	0.1	1.2	0.8	9.1
K2-141c	246393474	10.6	7.749	0.094	7.6	0.0	0.0	0.0	8.6
K2-140b	228735255	12.5	6.569	0.114	22.2	0.0	0.4	1.4	8.3
K2-229b	228801451	11.0	0.584	0.014	8.2	0.5	0.4	0.0	8.2

Table 1 *continued*

Table 1 (*continued*)

Identifier	EPIC ID	Kp (Mag)	Period (Days)	R_p/R_*	A_{Ref}	A_{Th}	A_{Ell}	A_{Dop}	SNR
K2-261b	201498078	10.5	11.633	0.053	6.3	0.0	0.1	0.2	7.9
K2-253 b	228809550	12.6	4.002	0.105	22.8	0.0	0.0	0.1	7.7
GJ 9827b	246389858	10.3	1.209	0.025	5.4	0.0	0.1	0.1	7.4
HD 89345	248777106	9.2	11.814	0.038	3.1	0.0	0.1	0.1	7.0
K2-121b	211818569	12.9	5.186	0.109	21.9	0.0	0.0	0.1	6.0
K2-137b	228813918	14.5	0.180	0.018	17.0	0.2	64.7	5.1	5.8
K2-157b	201130233	12.6	0.365	0.011	13.9	2.9	1.8	0.0	5.8
K2-99b	212803289	11.0	18.249	0.042	5.8	0.0	0.5	0.7	5.3
WASP-47e	206103150	11.8	0.790	0.014	8.1	0.6	1.0	0.1	5.1
HATS-36b	215969174	14.3	4.175	0.110	47.2	0.1	3.1	4.2	4.9
K2-113b	220504338	13.5	5.818	0.091	25.6	0.0	1.1	1.8	4.7
K2-132b	228754001	11.7	9.175	0.033	5.9	0.0	1.1	0.6	3.8
K2-45b	201345483	15.3	1.729	0.138	69.1	0.0	0.1	0.2	3.3

References for optical phase curves in (a) Močnik et al. (2018), (b) Malavolta et al. (2018), and (c) Dai et al. (2017b)

† All the detected phase curves planets are highlighted in bold.

For calculating the amplitude of the ellipsoidal variation A_{Ell} , we consider the formulation presented in Morris (1985):

$$A_{Ell} = \alpha_{Ell} \frac{M_p}{M_*} \left(\frac{1}{a/R_*} \right)^3 \sin^2 i, \quad (6)$$

$$\alpha_{Ell} = \frac{0.15(15+u)(1+g)}{(3-u)}, \quad (7)$$

where α_{Ell} is a constant characterizing tidal distortion, M_p is the mass of the planet, M_* is the mass of the star, a/R_* is the scaled semi-major axis, i is the inclination of the orbit, u is the linear limb-darkening parameter, and g is the gravity-darkening parameter. We determine the value of u and g by linearly interpolating among effective temperature, metallicity and $\log g$ and assuming turbulence of 2 km s^{-1} from the table provided by Claret & Bloemen (2011).

Similarly, the Doppler beaming effect (A_{Dop}) is modeled as following:

$$K = \left(\frac{2\pi G}{P} \right)^{1/3} \frac{M_p \sin i}{M_*^{2/3} \sqrt{1-e^2}}, \quad (M_p \ll M_*) \quad (8)$$

$$A_{Dop} = \alpha_D \frac{K}{c}, \quad (9)$$

where G is the gravitational constant, P is the period, M_p is the mass of the planet, M_* is the mass of the star. α_D is Doppler boosting factor, which is based on the proposition of Loeb & Gaudi (2003). For this work we use the empirical relation reported by Millholland

& Laughlin (2017) between the Doppler boosting coefficient (α_D) and effective stellar temperature (T_{eff}):

$$\alpha_D = 7.2 - (6 \times 10^{-4})T_{eff}. \quad (10)$$

Table 1 lists the ordered list of the 52 K2 exoplanets with the largest expected phase curve signal to noise, as obtained from Equation 2. It also lists the individual contributions of all four phase curve sources in parts per million (ppm), along with fundamental planetary and stellar parameters. Figure 1 displays predicted phase curve amplitude (A_{Eqv}) as a function of stellar magnitude. Nine among the list of presented targets have detected phase curves, six of which are identified in this work. Note that while we expect the ellipsoidal variation as well as Doppler amplitudes to be well constrained around our predicted values, the actual reflective as well as thermal components can be smaller by more than an order of magnitude. The choice of high geometric albedo is motivated primarily to cast a wide enough net not to miss any potential candidates. This, however, in turn leads to a high non-detection rate. Additionally, the observed light curve precision can be worse off than what is expected because of crowding, imperfect detrending, various systematics as well as the presence of the strong stellar activities. The combination of one or more of these factors means that for many of the planets listed in Table 1 we do not expect to detect their phase curves.

3. DATA PREPARATION

Phase curves signals are often times weak compared to other astrophysical signals present in the photometric time series. Filtering process to remove the is therefore a necessary step. By the time the final light curve is obtained, the data goes through multiple processing steps, each of which handles different aspects of the systematics. The official *Kepler* processing tool handles many of the detector and electronic effects (Jenkins et al. 2010). However, the pointing induced errors historically have been left up to the exoplanet community to address.

As a response, different pipelines were developed by research groups who have diverse research foci. For instance, Kepler Asteroseismic Science Operations Center (KASOC; Handberg & Lund 2014) pipeline was purposed for astero-seismic related studies, whereas for those interested in the stellar rotational period group developed independent pipelines (Angus et al. 2016). For the transit search, similarly different pipelines have been developed. For our work we consider two different pipelines, K2SFF (Vanderburg & Johnson 2014; Vanderburg et al. 2016) and EVEREST (Luger et al. 2016, 2018) primarily due to their ability to produce light curves with high precision. For our work, we have used the scatter of the phase folded light curve as the benchmark for selection criterion for any subsequent analysis. This was motivated by the reasoning that systematics is the single-handedly the most challenging hurdle standing in the way of the phase curve detection.

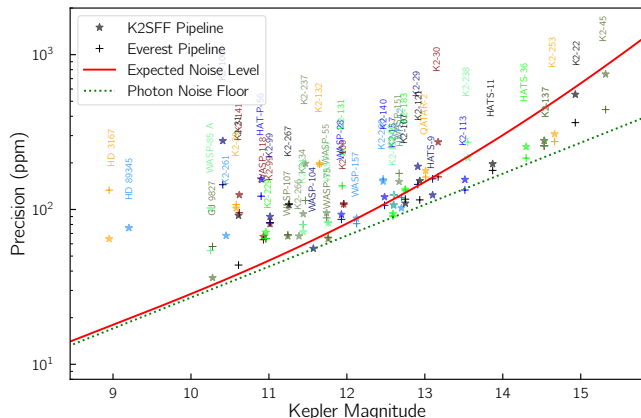


Figure 2. The observed precision for our targets compared to the expected noise level used for SNR estimation. The expected noise level underestimates the scatter for bright targets while generally overestimates the noise for the dimmer targets.

3.1. Detrending

Due to drift of the field in the rolling axis, which was periodically compensated for by thruster firings, pre-detrended light curves from *K2* exhibit a characteristic sawtooth pattern. In order to correct for such

patterns, different detrending algorithms and pipelines have been developed. For our work, we consider two different detrended light curves: EVEREST, and K2SFF, whose detrended light curves are publicly available at MAST Archive². We particularly focus on using these two pipelines due to their comprehensiveness and the quality of the final products the pipeline deliver. K2SFF light curves are available for all of our targets, whereas EVEREST is available for all of targets up until Campaign 13.

K2SFF is a parametric approach to detrending - decorrelating the motion of the centroid with the variation of the magnitude. On the other hand, EVEREST is a Gaussian process based detrending which models the intrapixel variation to produce the final light curve. Both of the methods produce light curves that are comparable in photometric precision (see Figure 2). Unfortunately, a comprehensive quantitative comparisons on the performance of these pipelines is beyond the scope of this paper. Light curves from both pipelines have been used successfully in different analyses. Dai et al. (2017b) used the light curve generated by EVEREST pipeline due to its higher precision whereas Malavolta et al. (2018) and Močnik et al. (2018) used some variation of K2SFF in producing the final light curve, which was then used for subsequent phase curve analyses.

The detrending removes most of the power injected at higher frequencies such as those introduced by thruster firing events, while at lower frequencies other long term systematics still can dominate (Van Cleve et al. 2016; Aranzana et al. 2018). Since the phase curve signals lie in the region which is usually well separated in the frequency domain from both of these effects, they are minimally distorted, and the treatment by these pipelines are sufficient in most of the cases. However, there are cases where these traditional *K2* pipelines often tend to fail, such as in crowded fields or for bright targets. This in turn has motivated the development of more specialized pipelines to handle crowding typically in a cluster environment (Libralato et al. 2016) or bright targets that can saturate the pixels (White et al. 2017). Such treatment usually is not necessary for most of our targets. At the same time, the light curves from these specialized pipelines are not as comprehensively available for all of the targets. Therefore, we limit our work with the light curves available from the two aforementioned pipelines.

In Figure 2, we compare the observed precision of the light curve against the expected precision. We found that the pre-flight prediction provided for *Kepler* tar-

² https://archive.stsci.edu/k2/data_search/search.php

gets³ overestimates the precision for the bright targets, whereas it underestimates the precision for the fainter targets. This error can be traced to the constant read noise error assigned to all of the targets calculated by assuming an aperture size of 20 pixels. For the bright targets the non-linear effects and background contamination poses worse problems than this calculation allows for. While a separate algorithm for detrending bright stars has been explored (White et al. 2017), there might be room for even more optimization. But overall, the assumed precision curve provides a good estimate of the precision expected for our targets.

3.2. Outliers Handling

The final light curve obtained by the pipelines needs further processing due to the presence of outliers. We initially remove all those data lying outside eight times the inter-quartile range. Following this, we mask out all the transit points found using the transit parameters reported in the NASA exoplanet database. We then locate the outliers through an iterative process excluding data that lie more than 3σ away from a highly sampled spline. This process is repeated once the light curve is folded, during which outliers occurring during transit events itself are removed. On average, this led to removal of around 2.5% of the original data across our targets.

Some of our targets show effects akin to thermal settling at the beginning of the data (see Figure 3). However, since these effects are not uniformly present in all our targets, we did not exclude these data points in our analysis. If multiple observations were available for a target, we combined all of the light curves available (as in the case of K2-34b) to produce the final light curve. *K2* light curves often have a gap typically of a few days at the middle of the observation for data downlinking. Such discontinuities are expected and well handled by the detrending pipelines as well as the filtering. For HATS-12 however, there is an abrupt offset at the middle of the observation (see Figure 3) which was observed in both of the detrended light curve. We correct for this apparent offset by modeling the continuum using linear regression at the break point, and applying the relevant offset to generate the final stellar continuum before filtering.

4. SIGNAL INJECTION RETRIEVAL TEST

In order to extract the phase curve, the stellar continuum has to be modeled out. A host of filtering techniques have been used in the past. Sometimes the stellar continuum exhibits little to no variation, therefore re-

quiring minimal pre-processing as in the case of TRES-2b (Barclay et al. 2012). However, for most of *K2* targets, filtering provides an opportunity not only to remove the stellar continuum, but also any uncorrected systematics. Thus, we explored suites of filtering techniques available to us, among which we focused particularly on three: spline, phasma and Butterworth.

1. Spline Filtering: Spline flattening is the most commonly used filtering technique for removing the stellar flux (Esteves et al. 2013; Shporer & Hu 2015; Angerhausen et al. 2015; Armstrong et al. 2016). Use of different degrees of polynomial or knotting intervals are common depending on the planetary period as well as the ability of the spline to model the stellar continuum. Splines essentially act as a low pass filter, and have been successfully used in a range of targets in the past. For this work, we adopt third degree polynomial knotted once every period of the planet.
2. Phasma: Phasma as a filtering method in the context of the phase curve was proposed in Jansen & Kipping (2018). Phasma in essence is a median filtering with window length set to the period of the planet. A similar implementation with a mean filter was also used. While easy to implement, phasma did not perform on par with spline filtering particularly among hot Jupiters (see Figure 4 and Figure 5).
3. Frequency filtering: Another method that has been used is harmonics based filtering (Quintana et al. 2013). In this work, we use the sixth order Butterworth filter as implemented in `scipy`⁴ with a bandpass between half the planetary frequency and 3.5 times the planetary frequency. The limits of the bandpass were partially motivated to preserve the third harmonics (Esteves et al. 2015), as well as decided through trial and error. Before filtering, we uniformly and linearly interpolate the light curve after masking the transit and occultation points. Overall, the performance of Butterworth filter performance was superior among the three filtering techniques studied in detail particularly among the hot Jupiters (see Figure 4, and Figure 5).

³ <https://keplergo.arc.nasa.gov/CalibrationSN.shtml>

⁴ `scipy.org`

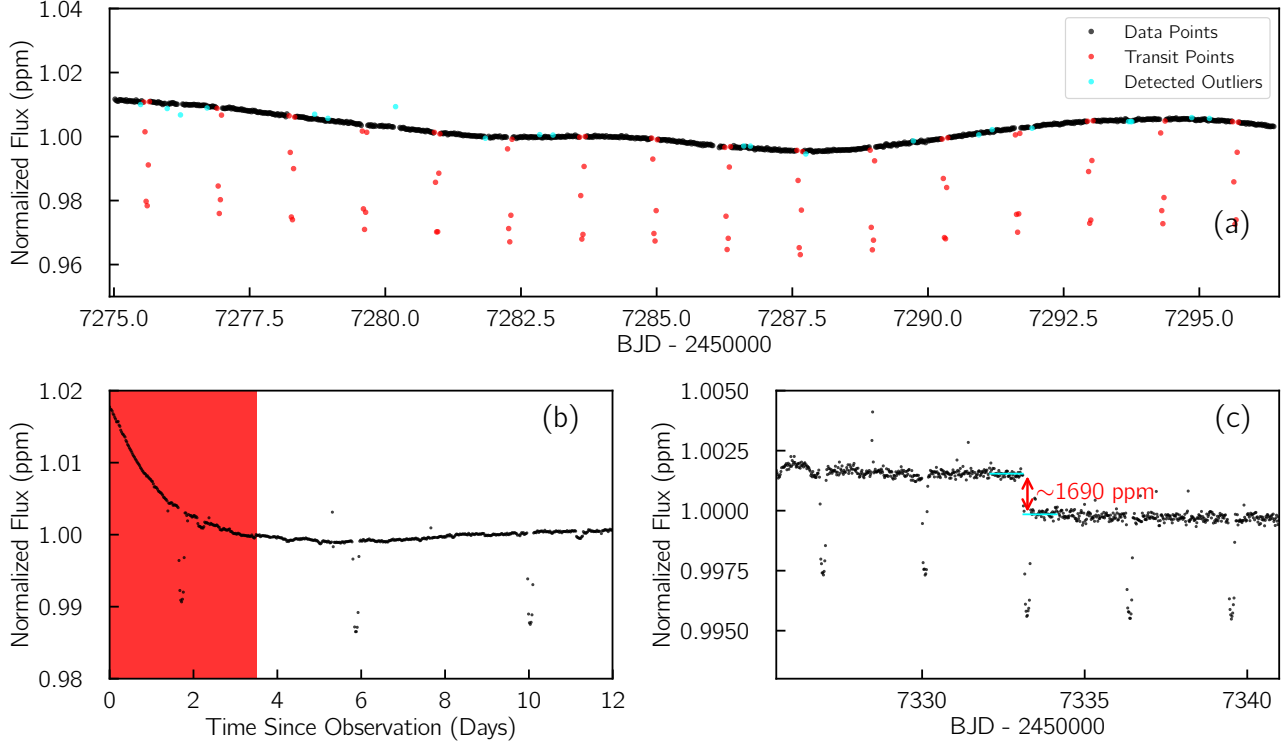


Figure 3. Figure showing different systematics in the detrended data. (a) Transit points and outliers detected in a portion of QATAR-2 EVEREST detrended light curve. (b) Potential systematic effects akin to thermal settling observed during the first few days of detrended WASP-47 EVEREST detrended data. (c) An abrupt change is observed in EVEREST detrended data for HATS-12b possibly due to a change in pixel responsivity. Note that a similar offset is spotted in K2SFF detrended data.

Table 2. Targets used for Signal Injection Test

Identifier	EPIC IDs
K2-31b	203089855, 203526723, 203758400, 204254456, 204529573
HATS-9b	214576141, 214963629, 215327780 215496957, 216068131
HATS-12b	215293111, 215310931, 215517702 215594041, 215677034
K2-107b	214402646, 215075353, 215542349 215771782, 215834357
K2-131b	201094825, 201094970, 201121210 201141186, 201164625
K2-106b	220197918, 220205426, 220209263 220228282, 220249101

For each system with detected phase curves, we download K2SFF and EVEREST detrended light curves of five target stars from the same campaign with similar magnitude and precision range after detrending. During the process of choosing the light curves for signal in-

jection test, targets exhibiting strong short term modulation (i.e. less than 10 days), exhibiting intrinsic variability, or having obvious uncorrected systematics were deliberately avoided. The list of targets used for signal injection-retrieval test are reported in Table 2. Among the 40 light curves we downloaded for our four hot Jupiter candidates, we injected the phase curve signals considering geometric albedos between 0.01 to 0.66 at a step-size of 0.01 and masses between 0.25 and 7.0 Jupiter mass with a step-size of 0.25 while using the reported transit parameters for the planets. We ran thus obtained light curves through our pipeline, and compared the final retrieved signal with the injected phase curve signal. The quick fits using Levenberg-Marquardt minimization showed that in most cases consistent parameters of albedo and mass to the injected signals can be retrieved. During these tests, we found the Butterworth filter outperforms both spline and phasma filtering among hot Jupiters (see Figure 4 and Figure 5). We also performed additional tests with phase offset signals, and Butterworth filter continued to outperform other two filters. For the ultra-short period super-Earths, we performed tests using parameters of K2-141, K2-131 and K2-106 for which we simulate phase curves with a reflective component with geometric albedo ranging between

0.01 to 0.8. For these latter set of planets, the performances of the different filtering techniques were comparable (see Figure 5).

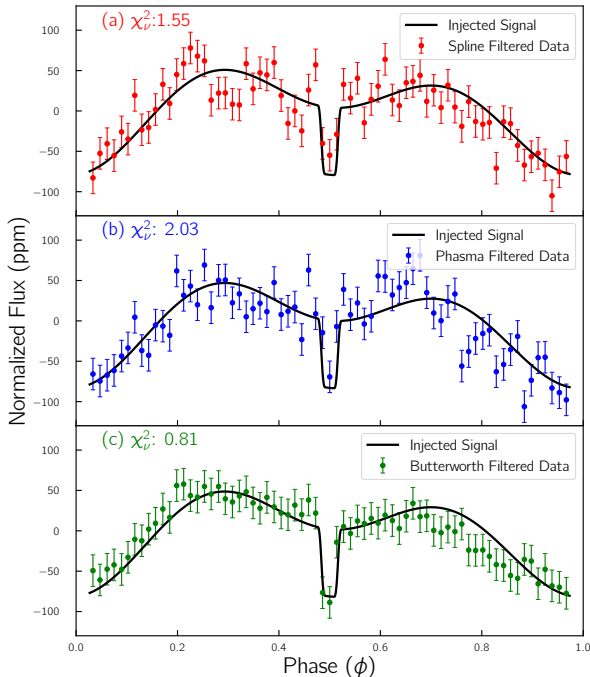


Figure 4. A random case of injected signal retrieved through (a) Spline Filtering, (b) Phasma Filtering (c) Butterworth bandpass Filtering. The error bars were scaled down accordingly to the bin-size from the calculated mean scatter.

Based on these tests, we have used Butterworth filtered light curves for all our hot Jupiter targets. The sixth order Butterworth filter allows us to be very selective in the frequency domain, but it can sometimes lead to ringing effects in the residuals visible for some of our targets. Despite this, we found the values of the retrieved parameters using Butterworth filter are in general more accurate compared to those obtained from two other filtering methods. We also explored the possibility of using narrower bandpass Butterworth filters however, overall such filters decreased the accuracy of the retrieved parameters in our signal injection test. On the other hand for the short period rocky planets (period less than a day) such as K2-131b or K2-106b, spline flattening light curves were used as its performance is comparable to Butterworth filter, and have already been shown to work robustly in a number of occasions.

One thing to keep in mind in interpreting our injection-retrieval test is that it has been heavily influenced by the parameters of planetary candidates among

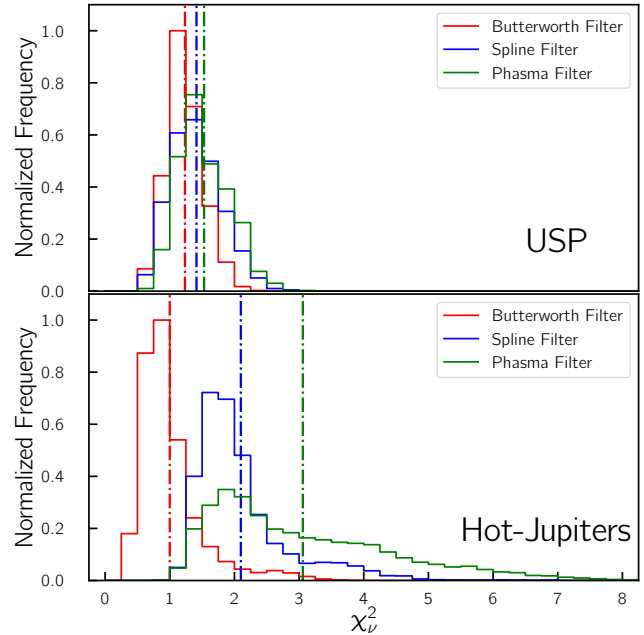


Figure 5. Top: Histogram of χ_ν^2 for the retrieved signal of the ultra-short period planets (USP). The performance of all three flattening methods are similar. Bottom: Histogram of χ_ν^2 for the retrieved signals observed for our samples of hot Jupiter targets. The mean value for shown with dotted lines χ_ν^2 was 1.00 for Butterworth filters, 2.09 for Spline Filters, and 3.06 for Phasma Filters. Among the filtering techniques, we found the Butterworth filter statistically performed the best.

which we detected the phase curves. Thus, the robustness of the process has not been tested in as wide range of scenarios. For instance, we have not taken into full consideration the stellar parameters such as stellar rotation which we find is one of the limiting factors in detecting phase curve (see §7). Similarly, while we have limited ourselves to three filtering techniques in this paper, there are a host of techniques available which we did not fully explore. For instance, some authors have pointed out the possibility of using Gaussian Processes (Serrano et al. 2018) for disentangling the planetary phase curves amid strong stellar rotation modulations. However, given the computational cost, the complexity of the model along with the possibility of overfitting the phase curves dissuaded us from diving too deep into this technique (Millholland & Laughlin 2017). In the future, we plan to explore a wider suite of filtering, and data analysis techniques which might allow us to improve on the process we introduce here.

5. MODEL FITTING

For all the targets where we detect phase curves, we simultaneously fit for the primary transit, secondary eclipse and phase curve. We set the period as noted in the NASA exoplanet archive to produce phase folded light curves. Since the planetary periods are both accu-

rately and precisely known through the transit method, this introduces negligible error. The simultaneous fit of the transit and the phase curves is primarily motivated to understand the cases with strong degeneracies among parameters as is the case of K2-31b. We initiate our MCMC model using the parameters reported in the discovery paper. For limb darkening, we use quadratic forms with uniform priors with range of 0.1 around the nearest values estimated by (Claret & Bloemen 2011). We similarly introduce priors in our MCMC for planetary period (P) and the scaled semi-major axis (a/R_*) parameters to only accept values that yields the stellar density (ρ_*) within 5σ of spectroscopically derived stellar density (Winn 2010):

$$\rho_* + k^3 \rho_p = \frac{3\pi}{GP^2} \left(\frac{a}{R_*} \right)^3, \quad (11)$$

where G is Gravitational constant, and ρ_p is the planetary density. We ignore the contribution from $k^3 \rho_p$ in our calculation. Additionally, we introduce a T_0 offset parameter, which allows for an offset in the time of the conjunction. Note that the final reported value of T_0 is calculated by appropriately combining this offset with the reported values in the original discovery paper.

We use the Mandel & Agol (2002) formalism as implemented in `batman` (Kreidberg 2015) in order to fit for the primary transit as well as the secondary eclipses. We supersample our light curve by a factor of 15, and set the exposure time to 29.4 minutes. For the phase curves, we used Bayesian Information Criteria (BIC) to choose the best model among three different models of phase curves: i) Thermal component with no significant nightside contribution ii) Thermal component with significant nightside contribution iii) Thermal component with a phase offset. In practice the first model was always preferred, which argues for more precise data. In the fitting schemes, we do not fit for phase variation during the transit, where we expect the transit to dominate the signal. For all of our models, we have used non-eccentric models inspired by the original discovery papers.

For exploring the parameter space, we used affine invariant MCMC implemented in `emcee` (Foreman-Mackey et al. 2013) running for 25,000 steps with 50 walkers. We use Gelman-Rubin statistics to ensure all of our MCMC converge. After the initial run, we compared the different models using Bayesian Information Criterion (BIC), and re-ran the best model for 50,000 step

by initializing our parameters around the best obtained values in the previous runs. We built the posterior distribution to estimate the error after removing the first 25,000 step of the data, and use the rest to estimate the error of the fit parameters. From posterior distribution, we report the median and 1σ confidence interval corresponding to 15.8th percentile and 84.2th percentile respectively. For some parameters such as planetary mass or equilibrium temperature, we propagate the error from the stellar parameters with the errors we estimate from the posterior distribution in our final reported parameters.

For all our models we consider circular orbits and expect the secondary eclipse to occur exactly at the half phase. We ignore the Rømer delay, and the effects of eccentricity. These choices were motivated by the precision of the data as well as the reporting of no significant eccentricities in the discovery papers. As for the temperature of the planet, we report the dayside temperature by numerically solving the following equation:

$$\Delta = A_g \left(\frac{R_p/R_*}{a/R_*} \right)^2 + \left(\frac{R_p}{R_*} \right)^2 \frac{\int B(T_{Day})R(\lambda)d\lambda}{\int B(T_{eff})R(\lambda)d\lambda}, \quad (12)$$

where Δ is the secondary eclipse depth, R_p/R_* is the scaled radius, a/R_* is the scaled semi-major axis, and B is Planck function which is convolved with the *Kepler* response function $R(\lambda)$. We solve Equation 12 for the geometric albedo (A_g), and assume the day-side contribution is a function of the geometric albedo using aforementioned López-Morales & Seager (2007) formalism introduced in Equation 5. In order to report the dayside temperature, we set the re-radiation factor to 1/2 and assume $A_B = 3/2A_g$ unless otherwise stated. Note this simple relation is not valid for planets in our solar system, and usually is likely to overestimate the value of the Bond Albedo (Dyudina et al. 2016). We also require the secondary eclipse depth to be strictly greater than or equal to the amplitude of the reflective and thermal component at phase 0.5. Similarly, the equilibrium temperature is calculated by setting the re-radiation factor to be 1/4.

We also ran the targets with the already reported phase curves of Qatar-2b, WASP-104b as well as K2-141b through our pipeline. In all three cases, we obtain results that are consistent with the reported phase curves. For QATAR-2b and WASP-104b, we obtained photometric masses of $3.20^{+0.37}_{-0.40} M_{Jup}$ and $0.94^{+0.26}_{-0.27} M_{Jup}$ consistent within 2σ of their RV-based masses $2.49 \pm 0.05 M_{Jup}$ (Bryan et al. 2012) and $1.27 \pm 0.05 M_{Jup}$ (Smith et al. 2014).

Table 3. Stellar and Planetary Parameters I

Parameter	Unit	K2-31	HATS-9	HATS-12	K2-107
Stellar Parameters					
M_*	M_\odot	0.91 ± 0.06^a	1.030 ± 0.039^b	1.489 ± 0.071^c	1.30 ± 0.14^d
R_*	R_\odot	0.78 ± 0.07^a	$1.503^{+0.101}_{-0.043}{}^b$	2.21 ± 0.21^c	1.78 ± 0.16^d
T_{eff}	K	5280 ± 70^a	5366 ± 70^b	6408 ± 75^c	6030 ± 120^d
[Fe/H]	dex	0.08 ± 0.05^a	0.340 ± 0.050^b	-0.100 ± 0.040^c	0.10 ± 0.10^d
$\log g_*$	cgs	4.60 ± 0.07^a	4.095 ± 0.038^b	3.923 ± 0.065^c	4.07 ± 0.10^d
u	-	0.6554^e	0.5467^e	0.5317^e	0.5723^e
g	-	0.4611^e	0.3200^e	0.2751^e	0.3280^e
Orbital Parameters					
Period	Days	1.257850 ± 0.000002^a	1.9153073 ± 0.000005^b	3.142833 ± 0.000011^c	3.31392 ± 0.00002^d
$T_0 - 2450000$	BJD	$2358.7092693^{+0.0000081}_{-0.0000082}$	6124.258947 ± 0.000017	6798.955614 ± 0.000024	$6928.059271^{+0.000017}_{-0.000016}$
R_p/R_*	-	$0.168^{+0.042}_{-0.023}$	$0.08414^{+(0.00014)}_{-0.00012}$	$0.06048^{+0.00056}_{-0.00042}$	$0.08335^{+0.00023}_{-0.00026}$
a/R_*	-	$5.66^{+0.10}_{-0.09}$	$4.556^{+0.011}_{-0.026}$	$5.47^{+0.19}_{-0.24}$	$5.890^{+0.082}_{-0.075}$
b	-	$1.022^{+0.053}_{-0.031}$	$0.065^{+0.065}_{-0.045}$	$0.29^{+0.12}_{-0.16}$	$0.7925^{+0.0074}_{-0.0082}$
Inclination	Deg	$79.61^{+0.51}_{-0.74}$	$89.29^{+0.55}_{-0.82}$	$87.0^{+1.8}_{-1.5}$	$82.27^{+0.18}_{-0.17}$
e	-	0 (assumed)	0 (assumed)	0 (assumed)	0 (assumed)
ω	Deg	90 (assumed)	90 (assumed)	90 (assumed)	90 (assumed)
u_1	-	$0.560^{+0.029}_{-0.051}$	$0.5300^{+0.0072}_{-0.0049}$	$0.3227^{+0.0091}_{-0.0053}$	$0.437^{+0.027}_{-0.019}$
u_2	-	$0.261^{+0.039}_{-0.062}$	$-0.012^{+0.017}_{-0.016}$	$0.236^{+0.013}_{-0.006}$	$0.100^{+0.030}_{-0.021}$
Phase Curve Parameters					
A_{Tot}	ppm	$12.27^{+0.85}_{-0.83}$	$11.6^{+2.3}_{-2.4}$	7.5 ± 1.9	$12.8^{+1.9}_{-2.0}$
T_{Day}	K	1860 ± 35	2100 ± 29	2240^{+82}_{-68}	2005^{+26}_{-27}
T_{eq}	K	1554 ± 29	1751 ± 24	$1849.^{+61}_{-52}$	1669^{+20}_{-21}
A_g	-	$0.008^{+0.013}_{-0.008}$	$0.027^{+0.015}_{-0.017}$	0.07 ± 0.04	0.102 ± 0.023
M_{RV}	M_{Jup}	1.774 ± 0.079^a	0.837 ± 0.029^b	2.38 ± 0.11^c	0.84 ± 0.08^d
M_{Phot}	M_{Jup}	2.09 ± 0.18	0.98 ± 0.16	$2.13^{+0.46}_{-0.43}$	$1.57^{+0.26}_{-0.27}$

^aAdopted from [Grziwa et al. \(2016\)](#)

^bAdopted from [Brahm et al. \(2015\)](#)

^cAdopted from [Rabus et al. \(2016\)](#)

^dAdopted from [Eigmüller et al. \(2017\)](#)

^eLinear limb-darkening (u) and gravity-darkening (g) coefficients interpolated from [Claret & Bloemen \(2011\)](#)

5.1. *K2-31b*

Given the short period, high mass and large scaled radius, K2-31b was the best candidate among *K2* discovered planets to have a detectable phase curve. Our analysis of the data indeed shows the presence of a robust phase curve with all of the components present. K2-31b is a grazing hot Jupiter with mass of $\sim 1.8 M_{Jup}$ discovered by [Grziwa et al. \(2016\)](#). Due to the grazing nature of the transit, the planet radius is not very precisely determined because of the degeneracy between the

inclination and the scaled planetary radius. Our MCMC yielded the scaled radius of the planet of $0.168^{+0.042}_{-0.023}$, which assuming a host star of radius $0.78 R_\odot$ translates into physical radius of $1.28^{+0.32}_{-0.17} R_{Jup}$.

For our analysis, we use the EVEREST detrended light curve and obtain a mass of $2.09 \pm 0.18 M_{Jup}$ consistent with the RV-based mass of 1.774 ± 0.079 reported in the discovery paper M_{Jup} within 2σ . [Grziwa et al. \(2016\)](#) points out that due to its grazing nature which is often interpreted as eclipsing binaries, planets like K2-31b are usually neglected for RV follow-up. But we show

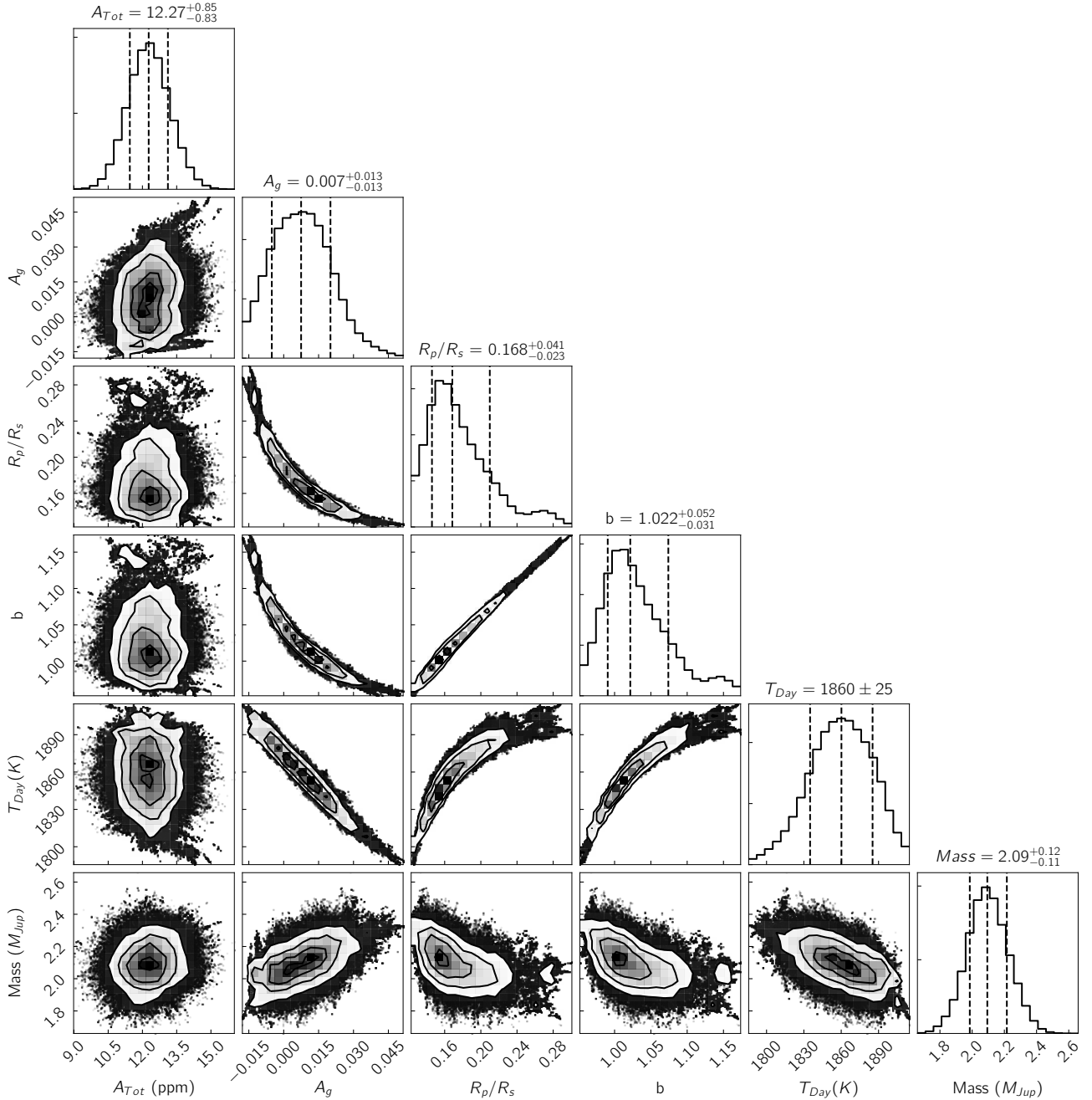


Figure 6. Corner plot showing the posterior distribution and co-variance among different fit parameters of K2-31b. A strong degeneracy is present among the scaled radius (R_p/R_*), geometric albedo (A_g), impact parameter (b), and day-side temperature (T_{Day}), while the mass of the planet exhibits minimal correlation with most of the parameters. The errors from the stellar parameters have not been propagated.

here that the planetary nature could indeed have been validated by estimating mass through the optical phase curve. In the discovery paper, [Grziwa et al. \(2016\)](#) constrains the upper limit on the geometric albedo of K2-31b at 0.40, due to the absence of any visible secondary eclipse. By fitting for the whole phase curve, we are able to constrain the geometric albedo to $0.008^{+0.013}_{-0.008}$, a dark planet even by the standard of hot Jupiters ([Esteves et al. 2015](#); [Angerhausen et al. 2015](#)). Yet, the

grazing nature of the transit leads to strong degeneracy among parameters (see [Figure 6](#)), as well as the underlying assumptions for the thermal emission and the Bond albedo leaves room for unaccounted systematic errors for such estimation. The degeneracy among different parameters, however is not as strong in the observed photometric mass.

5.2. HATS-9b

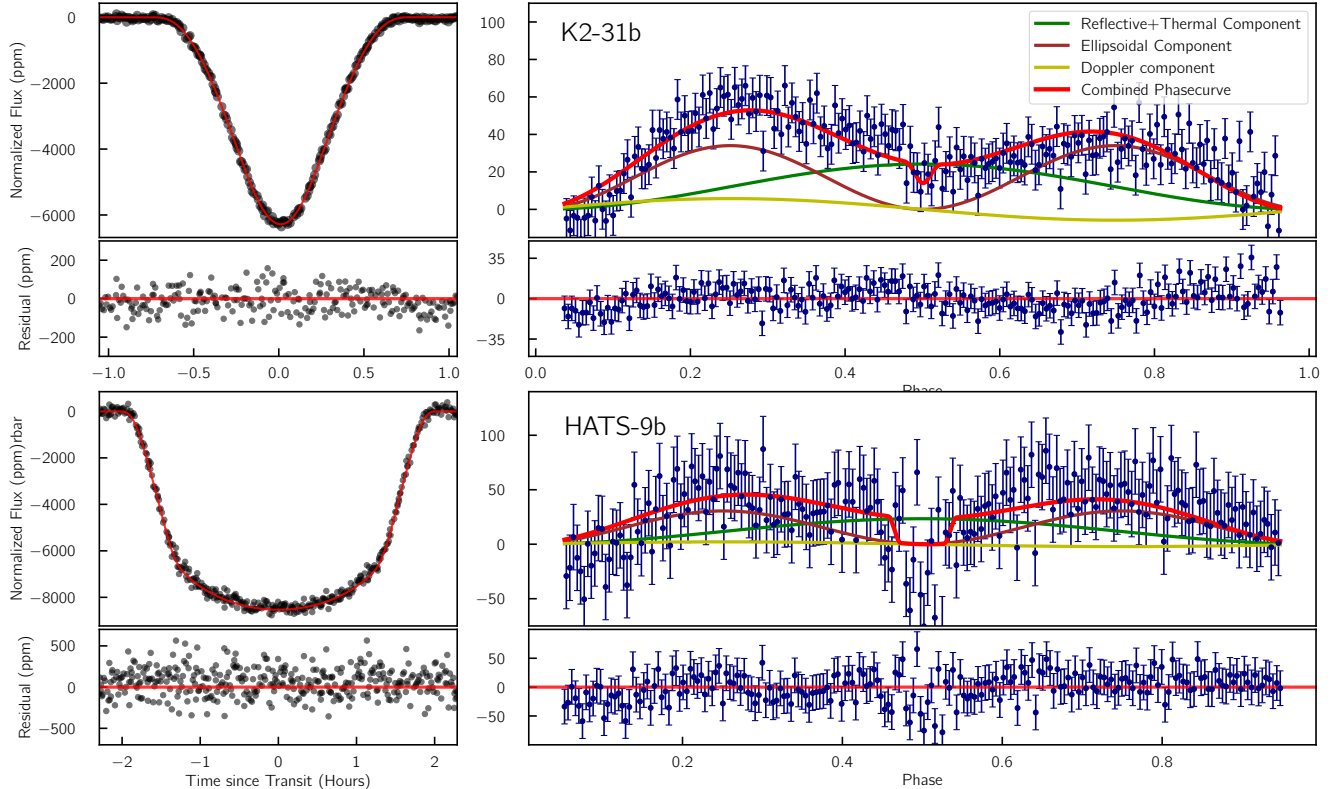


Figure 7. Upper-left: Transit fit using the best fit parameter for K2-31b and the residual. Upper-right: Phase curve signal using the best obtained parameter for K2-31b with different components. The data was binned to have a total number of bins of 200, thus each bin size corresponds to 0.14 hours. Lower-left: Transit fit using the best fit parameter for HATS-12b and the residual. Lower-right: Phase curve signal using the best set of visualization in HATS-9b with different components and its residual. The data was binned to have a total number of bins of 200, thus each bin size corresponds to 0.21 hours.

HATS-9b is a hot Jupiter that was discovered in the Campaign 7 *K2* field (Brahm et al. 2015). Bayliss et al. (2018) updated the system parameters using the *K2* lightcurve, however did not report the phase curve or the secondary eclipse. We use K2SFF detrended light curve for this particular analysis given its precision, and in examining the light curve for the potential phase curve, we detect the ellipsoidal variation for HATS-9b which yielded a photometric mass of $0.98 \pm 0.16 M_{\text{Jup}}$ consistent with the reported RV mass of $0.837 \pm 0.029 M_{\text{Jup}}$ within 1σ . Similarly, the secondary eclipse for HATS-9b is one of the more prominent ones among our targets which yielded a geometric albedo of $0.027^{+0.015}_{-0.017}$. The fit using the best parameters is shown in Figure 7, and the corresponding parameters are reported in Table 3.

5.3. HATS-12b

HATS-12b (Rabus et al. 2016) was another hot Jupiter discovered in the *K2* Campaign 7 field. An abrupt jump in the data was observed in both detrended light curves around BJD - 2457333.1 (see Figure 3), possibly due to a change in the pixel responsivity (Jenkins et al. 2010). We use K2SFF detrended light curves for the analysis, and corrected for the jump by using a linear regression

at the break point. Marked as one of the promising targets using our SNR metric, we see distinct phase curve emerge in the phase folded light curve. The phase curves exhibits particularly prominent ellipsoidal variation, fitting for which leads to a mass of $2.13^{+0.46}_{-0.43} M_{\text{Jup}}$ consistent with the reported RV mass of $2.38 \pm 0.11 M_{\text{Jup}}$ within 1σ . The good agreement comes with a little surprise given HATS-12 has a stellar mass of $1.489 \pm 0.071 M_{\odot}$, which lies above $1.4 M_{\odot}$, a threshold beyond which the tidal-equilibrium approximation for ellipsoidal variation is not expected to strictly hold (Pfahl et al. 2008). Similarly, we find the geometric albedo is 0.07 ± 0.04 , typical for hot Jupiters. The fit using the best set of parameters is shown in Figure 8, and the corresponding parameters are reported in Table 3.

5.4. K2-107b

K2-107b was reported in Eigmüller et al. (2017). A few nearby companions were detected with high resolution imaging, which are positioned in the *K2* aperture, however the combined dilution factor correction due to these companion is 0.005 ± 0.001 , therefore negligible for the calculation we are considering. We use the EVEREST detrended light curve for the fitting purposes, which

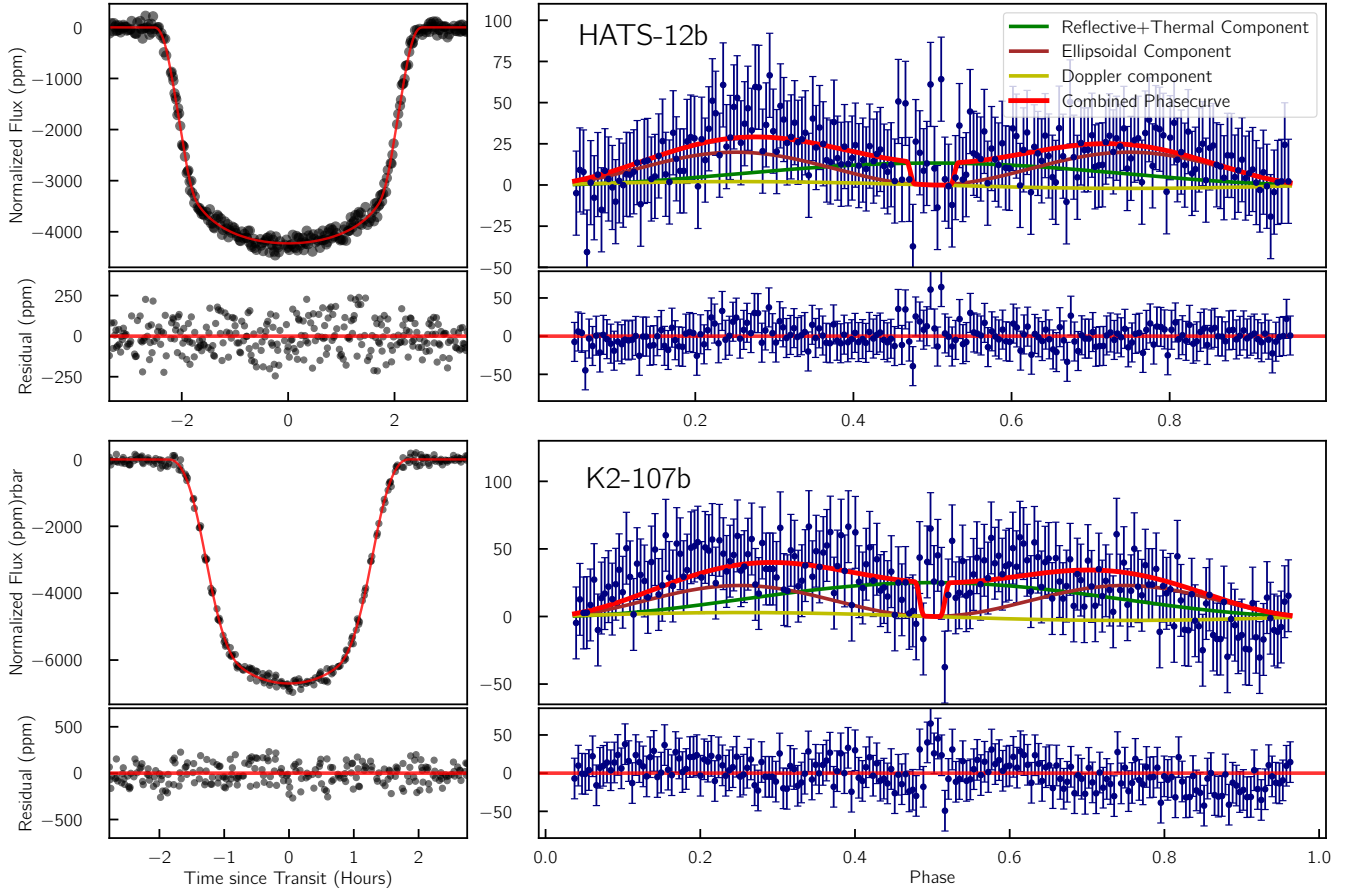


Figure 8. Upper-left: Transit fit using the best fit parameter for HATS-12b and its residual. Upper-right: Phase curve signal using the best obtained parameter for HATS-12b with different components. The data was binned to have a total number of bins of 200, thus each bin size corresponded to 0.34 hours. Lower-left: Transit fit using the best fit parameter obtained for K2-107b and its residual. Lower-right: Phase curve signal using the best set of visualization in K2-107b with different components and its residual. The data was binned to to have a total number of bins of 200, thus each bin size corresponds to 0.37 hours.

yields a photometric mass of $1.57^{+0.26}_{-0.27} M_{\text{Jup}}$, which is within 3σ of RV mass reported at $0.84 \pm 0.08 M_{\text{Jup}}$. The estimated geometric albedo is 0.102 ± 0.023 . The fit of K2-107b is shown in Figure 8, and the parameters are reported in Table 3.

5.5. K2-131b

K2-131b is an ultra-short period planet with a period of 0.3693 days reported in Dai et al. (2017a). For this work, we use the light curve from EVEREST pipeline, and only from the second half of Campaign 10 as the first half of the data shows strong systematic effects. In the phase folded data, we detect the secondary eclipse at 25.4 ± 8.2 ppm. We fit for reflective and thermal component, and not for ellipsoidal or Doppler beaming due to negligible expected contributions. Unlike for the hot Jupiters in our lists, we use an altered relation between the geometric albedo and Bond Albedo as $A_B = A_g$. Unless this modification is implemented, the geometric albedo values converge to nonphysical negative values. This deviation from the traditional Lambertian relation

($A_B = \frac{3}{2}A_g$) in fact is expected as it tends to overestimate the Bond Albedo (Dyudina et al. 2016). The fits showing the best obtained parameters are shown in Figure 9, and the parameters are reported in Table 4.

5.6. K2-106b

K2-106 is a multi-planetary system with an ultra short period planet with period of 0.57133 days. It was first identified as a candidate in Adams et al. (2017), and subsequent RV campaigns verified the planetary nature of the signal with mass reported in Guenther et al. (2017) and Simukoff et al. (2017). For our analysis, we adopted the values from the latter. We detect the secondary eclipse at $23.5^{+4.9}_{-5.1}$ ppm. Reflective and thermal component constitute the dominant part of the phase curve (see Figure 9), and like K2-131b, we do not fit for either ellipsoidal variation or Doppler beaming due to negligible expected contributions. In order to estimate the temperature, we similarly use the modified relation i.e. $A_B = A_g$. The resulting values are reported in Table 4, while the fit itself is shown in Figure 9.

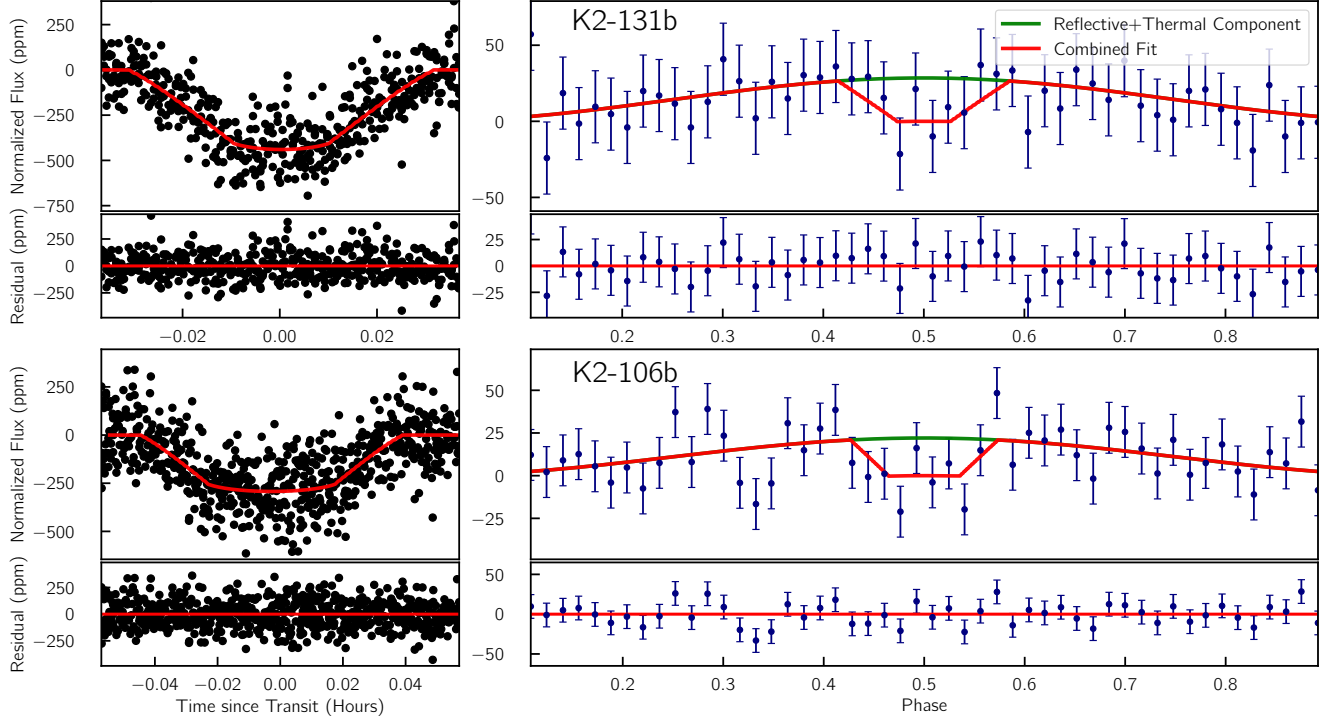


Figure 9. Upper-right: Transit fit using the best parameter for K2-131b. Upper-left: Phase curve modulation showing reflective and thermal component in K2-131b with a secondary eclipse depth at 25.4 ± 8.2 ppm. A total of 50 bins are used which corresponds to bin size of 0.14 hours. Lower-right: Lower-left: Phase curve modulation showing reflection and thermal component modulation in the folded light curve of K2-106b with a secondary eclipse depth at $23.5^{+4.9}_{-5.1}$ ppm. A total of 50 bins are used which corresponds to bin size of 0.14 hours.

6. SECONDARY ECLIPSE

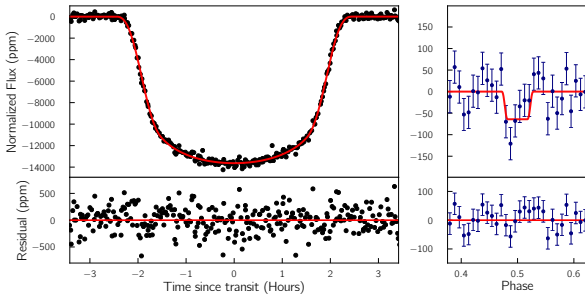


Figure 10. Transit fit (left) is shown for HATS-11b using best fit parameters which are reported in Table 4. The secondary eclipse (right) is detected at 62 ± 12 ppm.

To our knowledge, K2-260b is the only planet up until now with a robust secondary eclipse detection among the planets discovered by *K2* (Johnson et al. 2018). Since secondary eclipses characterize the geometric albedo as well as the temperature contrast just through observation of the depth of secondary eclipse alone, it is less prone to periodic or quasi-periodic noises. We therefore uniformly look for secondary eclipse signals for all planets reported in Table 1.

For our secondary eclipse detection pipeline, we

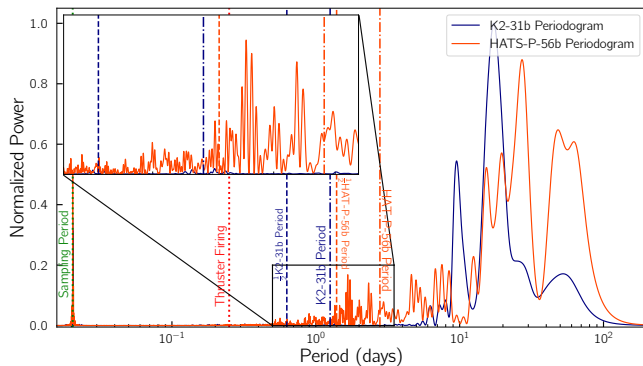
masked the range of data at transit as well as the phase of 0.5, where we estimate the secondary eclipse to occur. To the rest, we fitted a third degree polynomial with a length of 0.75 days and phase folded the data to build up the signal. The rest of the pipeline includes the same iterative outliers detection technique as was implemented for the phase curves. In this fashion, we detected secondary eclipse in K2SFF light curves of HATS-11b at 62 ± 12 ppm (see Figure 10). We use the depth to solve for the dayside temperature as well as the albedo for HATS-11b. The fit parameters are reported in Table 4.

The detection of a secondary eclipse without the phase curve, as is the case for HATS-11b, raises an interesting question - why is there a secondary eclipse without a phase curve? HATS-11b has an easy-to-model stellar continuum that makes extracting a phase curve rather easy, although the signal may have been distorted during one of the many data processing steps. It also could be that the source of phase curve is predominantly thermal, and an efficient heat transportation between day and night-side significantly weakens the phase curve signal. Another explanation could be that the planetary atmosphere at the depth the phase curve probes is rotating at a pseudo-synchronous rate (Adams & Laughlin 2018) washing out the signal as we phase fold the light curve. Note using EVEREST light curve for HATS-11b, which

has comparable precision level as the K2SFF light curve, the secondary eclipse depth was detected at the level of 36 ± 11 ppm, still a 3σ detection. It still lacks a robust phase curve.

7. NON-DETECTION

For the most part, our formulated metric is expected to perform as well as, if not better than, the previously used metrics such as $a/R_* < 10$ in [Esteves et al. \(2013\)](#), and $R_p > 4R_\oplus$, $P < 10$ days and $V_{\text{mag}} < 15$ in [Angerhausen et al. \(2015\)](#). However, our precision approximation relation deviates from the actual observed value for fainter stars, which in the future could be improved by using the empirically obtained noise floor. Similarly our calculation of SNR ratio could underestimate the signal for small period planets due to potentially non-negligible contribution from tidal heating of the planets.



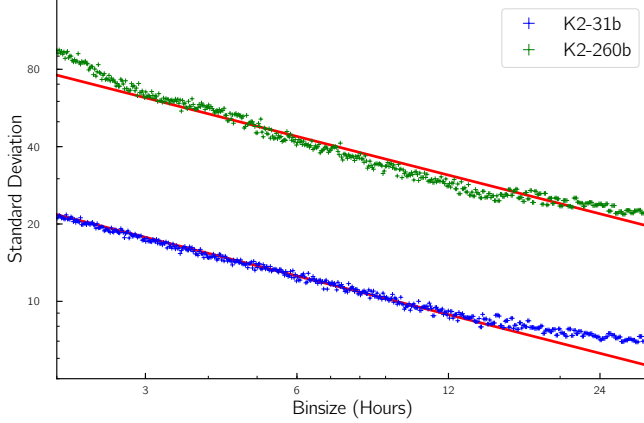


Figure 12. Observed RMS vs the bin size in the residual obtained by fitting phase curve models in K2-260b and K2-31b. Binning in K2-31b follows the expected power law of 0.5, whereas for K2-260b strongly deviates from it. The red lines are idealized cases drawn for both data sets.

spin-orbit resonance. Despite reporting a prominent secondary eclipse, [Johnson et al. \(2018\)](#) did not report the phase curve for the planet. We ran our pipeline, and fitted the phase folded light curve, which however yielded a mass inconsistent with reported RV value by more than 3σ . The residuals from the fit show the correlated noise which stand out in RMS vs bin size plots compared to the residuals from the targets such as K2-31b for which the phase curve is reported (see [Figure 12](#)). All of our phase curve targets have residuals that closely follow the expected the power law.

8.3. Ultra-Short Period Planet

With our discovery, K2-131b and K2-106b now join the group of other ultra-short planets such as Kepler-78 ([Sanchis-Ojeda et al. 2013](#)), Kepler-10b ([Esteves et al. 2013](#)), 55-Cnc-e ([Demory et al. 2016](#)) and K2-141b ([Malavolta et al. 2018](#)) with a detected secondary eclipse. Note all of these planets are rocky super-Earths with high densities and high geometric albedos possibly due to the presence of refractory surfaces. There

might be non-negligible additional source of heating such as tidal heating present in these systems which scales strongly with distance from the host star (a) and eccentricity (e) as follows:

$$H = \frac{63}{4} \frac{(GM_*)^{3/2} M_* R_p^5}{Q_p} a^{-15/2} e^2 \quad (13)$$

where H is the tidal heating rate, M_* is the stellar mass, R_p is the planetary radius, and Q_p is the tidal dissipation parameter ([Jackson et al. 2008](#)). The fact that most of these planets are multi-planetary system suggest mechanisms similar to Io as a Galilean moon of Jupiter may also be acting on these planets ([Peale et al. 1979](#); [Demory et al. 2016](#)). While tidal heating will increase the overall equilibrium temperature of these planets, thereby increasing the nightside contribution, the precision of *K2* data does not allow us to explore such effects. Yet, asymmetries between the day and nightside can still occur due to mechanisms such as volcanism ([Gelman et al. 2011](#)), which would also contribute to the phase curve signals.

8.4. Spectroscopic Follow-Up

Phase curves can be used to infer the existence of atmospheres for the close-in hot planets through the detection of the offset of the phase curve peaks ([Shporer & Hu 2015](#); [Demory et al. 2016](#); [Angelo & Hu 2017](#)). Similarly, the geometric albedo can be linked to atmospheric processes such as clouds, which are known to play important roles in the transmission spectrum ([Kreidberg et al. 2014](#); [Sing et al. 2016](#)). Currently, there are only a few targets with reported geometric albedo which have been followed up with spectroscopic observation. However, this will drastically change as *TESS* discovers a large sample of optimal targets. This could enable screening out the best planetary candidates for the follow-up atmospheric studies using the geometric albedo as a guideline.

Table 4. Stellar and Planetary Parameters II

Parameter	Unit	K2-131b	K2-106b	HATS-11b
Orbital Parameters				
M_*	M_\odot	0.84 ± 0.03^a	0.92 ± 0.03^b	1.000 ± 0.060^c
R_*	R_\odot	0.81 ± 0.03^a	0.95 ± 0.05^b	1.444 ± 0.057^c
T_{eff}	K	5200 ± 100^a	5496 ± 46^b	6060 ± 150^c
[Fe/H]	dex	-0.02 ± 0.08^a	0.06 ± 0.03^b	-0.390 ± 0.060^c
$\log g_*$	cgs	4.62 ± 0.10^a	4.42 ± 0.05^b	4.118 ± 0.026^c
u	-	0.6604^d	0.6294^d	0.5467^d

Table 4 continued

Table 4 (*continued*)

Parameter	Unit	K2-131b	K2-106b	HATS-11b
g	-	0.4737 ^d	0.4181 ^d	0.3199 ^d
Orbital Parameters				
Period(Days)	Days	0.3693038±0.000009 ^a	0.571336±0.000020 ^b	3.6191613±0.0000099 ^c
$T_0 - 2450000$	BJD	6226.437335 ^{+0.00084} _{-0.00090}	6226.43156±0.00069	6574.965605 ^{+0.000046} _{-0.000045}
R_p/R_*	-	0.01968 ^{+0.0016} _{-0.0006}	0.01584 ^{+0.00086} _{-0.00036}	0.10707 ±0.00013
a/R_*	-	2.61 ^{+0.23} _{-0.58}	2.73 ^{+0.16} _{-0.47}	7.006 ^{+(0.010)} _{-0.015}
e	-	0 (fixed)	0 (fixed)	0 (fixed)
ω	-	90 (fixed)	90 (fixed)	0 (fixed)
b	-	0.43 ^{+0.32} _{-0.31}	0.37 ^{+0.31} _{-0.25}	0.036 ^{+0.039} _{-0.025}
Inc	Deg	80 ⁺⁷ ₋₁₂	82.3 ^{+5.4} _{-9.7}	89.70 ^{+0.21} _{-0.32}
u_1	-	0.511 ^{+0.077} _{-0.054}	0.451 ^{+0.072} _{-0.063}	0.383 ^{+0.007} _{-0.008}
u_2	-	0.141 ^{+0.077} _{-0.056}	0.228 ^{+0.068} _{-0.068}	0.2000 ^{+0.0087} _{-0.0039}
Secondary Eclipse Fit Parameters				
Δ	ppm	25.4±8.2	23.5 ^{+4.9} _{-5.1}	62±12
A_g	-	0.27 ^{+0.31} _{-0.27}	0.60 ^{+0.21} _{-0.44}	0.249 ^{+0.057} _{-0.058}
T_{Day}	K	2670 ⁺⁸²⁰ ₋₄₁₀	2370 ⁺⁷⁷⁰ ₋₄₂₀	1841 ⁺⁶¹ ₋₆₇
T_{Eq}	K	2010 ⁺⁴⁵⁰ ₋₂₇₀	1860 ⁺⁴²⁰ ₋₃₈₀	1428 ⁺⁴⁴ ₋₄₉

^a Adopted from Dai et al. (2017a)

^b Adopted from Simukoff et al. (2017)

^c Adopted from Rabus et al. (2016)

^d Interpolated from Claret & Bloemen (2011)

8.5. Future Prospects

With the launch of *TESS* and the up-coming future missions like CHaracterising ExOPlanet Satellite (*CHEOPS*; Broeg et al. 2013) James Webb Space Telescope (*JWST*; Beichman et al. 2014), PLAnetary Transits and Oscillation of stars (*PLATO*; Rauer et al. 2014), and Atmospheric Remote-sensing Exoplanet Large-survey (*ARIEL*; Tinetti et al. 2016), there will be plentiful opportunities in the future for phase-curves studies. In fact, the phase curve of WASP-18b has already been reported in Sector 2 *TESS* data (Shporer et al. 2018), and more will definitely be detected over the course of the mission. These studies will allow an unprecedented opportunity to learn about exoplanet atmospheres, while allowing us to refine our models with more precise data, and potentially disentangle the often degenerate reflective and the thermal components (Placek et al. 2016).

9. CONCLUSION

We have significantly increased the number of phase curves discovered by *K2* with four hot Jupiters' phase

curves that yield photometric masses within 3σ of the reported RV-based masses, and two additional short period super-Earths with 3σ level secondary eclipse detections along with corresponding phase curves. The availability of the precise light curves as well as the use of a more aggressive filtering procedure tested with signal injection facilitated in our venture. The consistency of the obtained mass, although for a small but non-negligible number of planets, raises the possibility of developing a tool for preliminary planetary signal validation for *TESS* candidates. As we stand on the cusp of discovering many more planets, and will re-observe many of the hot Jupiters, an opportunity will be presented to refine our phase curve models, build a larger sample of planets with detected phase curves and open up novel lines of inquiry. Such possibilities and others should strongly motivate the pursuit of the phase curves, as they will provide preliminary atmospheric characterization and mass estimation for many of the systems without investing any additional resources.

Acknowledgments: This work includes data taken by

K2, and the final detrended light curves from *K2SFF* as well as EVEREST pipeline. Authors would like to thank Dr. Andrew Vanderburg for discussion on *K2SFF* pipeline products, as well as Dr. Rodrigo Luger in regards to discussion on EVEREST pipeline. P. Niraula would like to gratefully acknowledge the support of the Grayce B. Kerr Fellowship Fund. D. Serindag acknowl-

edges support from the European Research Council under the European Union’s Horizon 2020 research and innovation program under grant agreement No. 694513.

Software: `batman` (Kreidberg 2015), `emcee` (Foreman-Mackey et al. 2013), `gatspy` (VanderPlas & Ivezić 2015), `lmfit` (Newville et al. 2016), `matplotlib` (Hunter 2007).

REFERENCES

- Adams, A. D., & Laughlin, G. 2018, *AJ*, 156, 28
- Adams, E. R., Jackson, B., Endl, M., et al. 2017, *AJ*, 153, 82
- Angelo, I., & Hu, R. 2017, *AJ*, 154, 232
- Angerhausen, D., DeLarme, E., & Morse, J. A. 2015, *PASP*
- Angus, R., Foreman-Mackey, D., & Johnson, J. A. 2016, *ApJ*, 818, 109
- Aranzana, E., K rding, E., Uttley, P., Scaringi, S., & Bloemen, S. 2018, *MNRAS*, 476, 2501
- Armstrong, D. J., de Mooij, E., Barstow, J., et al. 2016, *Nature Astronomy*, 1, 0004
- Baglin, A., Auvergne, M., Barge, P., et al. 2002,
- Barclay, T., Huber, D., Rowe, J. F., et al. 2012, *ApJ*, 761, 53
- Bayliss, D., Hartman, J. D., Zhou, G., et al. 2018, *AJ*, 155, 119
- Beichman, C., Benneke, B., Knutson, H., et al. 2014, *PASP*, 126, 1134
- Borucki, W. J., Koch, D., Basri, G., et al. 2010, *Science*, 327, 977
- Brahm, R., Jord n, A., Hartman, J. D., et al. 2015, *AJ*, 150, 33
- Broeg, C., Fortier, A., Ehrenreich, D., et al. 2013, *European Physical Journal Web of Conferences*, 47, 03005
- Bryan, M. L., Alsubai, K. A., Latham, D. W., et al. 2012, *ApJ*, 750, 84
- Claret, A., & Bloemen, S. 2011, *A&A*, 529, A75
- Cowan, N. B., Chayes, V., Bouffard,  ., Meynig, M., & Haggard, H. M. 2017, *MNRAS*, 467, 747
- Dai, F., Winn, J. N., Gandolfi, D., et al. 2017, *AJ*, 154, 226
- Dai, F., Winn, J. N., Yu, L., & Albrecht, S. 2017, *AJ*, 153, 40
- Demory, B.-O., de Wit, J., Lewis, N., et al. 2013, *ApJL*, 776, L25
- Demory, B.-O., Gillon, M., de Wit, J., et al. 2016, *Nature*, 532, 207
- de Wit, J., Lewis, N. K., Knutson, H. A., et al. 2017, *ApJL*, 836, L17
- Dyudina, U., Zhang, X., Li, L., et al. 2016, *ApJ*, 822, 76
- Eigm ller, P., Csizmadia, S., Endl, M., et al. 2018, *MNRAS*, 480, 3864
- Eigm ller, P., Gandolfi, D., Persson, C. M., et al. 2017, *AJ*, 153, 130
- Esselstein, R., Aigrain, S., Vanderburg, A., et al. 2018, *ApJ*, 859, 167
- Esteves, L. J., De Mooij, E. J. W., & Jayawardhana, R. 2013, *ApJ*, 772, 51
- Esteves, L. J., De Mooij, E. J. W., & Jayawardhana, R. 2015, *ApJ*, 804, 150
- Faigler, S., Kull, I., Mazeh, T., et al. 2015, *ApJ*, 815, 26
- Faigler, S., & Mazeh, T. 2015, *ApJ*, 800, 73
- Faigler, S., Mazeh, T., Quinn, S. N., Latham, D. W., & Tal-Or, L. 2012, *ApJ*, 746, 185
- Faigler, S., Tal-Or, L., Mazeh, T., Latham, D. W., & Buchhave, L. A. 2013, *ApJ*, 771, 26
- Foreman-Mackey, D., Hogg, D. W., Lang, D., & Goodman, J. 2013, *PASP*, 125, 306
- Gelman, S. E., Elkins-Tanton, L. T., & Seager, S. 2011, *ApJ*, 735, 72
- Gilliland, R. L., Chaplin, W. J., Dunham, E. W., et al. 2011, *ApJS*, 197, 6
- Grziwa, S., Gandolfi, D., Csizmadia, S., et al. 2016, *AJ*, 152, 132
- Guenther, E. W., Barrag n, O., Dai, F., et al. 2017, *A&A*, 608, A93
- Handberg, R., & Lund, M. N. 2014, *MNRAS*, 445, 2698
- Harrington, J., Hansen, B. M., Luszcz, S. H., et al. 2006, *Science*, 314, 623
- Hermes, J. J., G nsicke, B. T., Kawaler, S. D., et al. 2017, *ApJS*, 232, 23
- Hidalgo, D., Alonso, R., & Palle, E. 2018, arXiv:1810.07495
- Howell, S. B., Sobeck, C., Haas, M., et al. 2014, *PASP*, 126, 398
- Huang, C. X., Hartman, J. D., Bakos, G.  ., et al. 2015, *AJ*, 150, 85
- Huber, K. F., Czesla, S., & Schmitt, J. H. M. M. 2017, *A&A*, 597, A113
- Hunter, J. D. 2007, *Computing in Science and Engineering*, 9, 90
- Jackson, B., Barnes, R., & Greenberg, R. 2008, *MNRAS*, 391, 237
- Jansen, T., & Kipping, D. 2018, *MNRAS*, 478, 3025
- Jenkins, J. M., Caldwell, D. A., Chandrasekaran, H., et al. 2010, *ApJL*, 713, L87
- Johnson, M. C., Dai, F., Justesen, A. B., et al. 2018, *MNRAS*, 481, 596
- Knutson, H. A., Charbonneau, D., Allen, L. E., et al. 2007, *Nature*, 447, 183
- Kreidberg, L., Bean, J. L., D sert, J.-M., et al. 2014, *Nature*, 505, 69
- Kreidberg, L. 2015, *PASP*, 127, 1161
- Libralato, M., Nardiello, D., Bedin, L. R., et al. 2016, *MNRAS*, 463, 1780
- Lillo-Box, J., Barrado, D., Henning, T., et al. 2014, *A&A*, 568, L1
- Loeb, A., & Gaudi, B. S. 2003, *ApJL*, 588, L117
- L pez-Morales, M., & Seager, S. 2007, *ApJL*, 667, L191
- Luger, R., Agol, E., Kruse, E., et al. 2016, *AJ*, 152, 100
- Luger, R., Kruse, E., Foreman-Mackey, D., Agol, E., & Saunders, N. 2018, *AJ*, 156, 99
- Lund, M. N., Chaplin, W. J., Casagrande, L., et al. 2016, *PASP*, 128, 124204
- Malavolta, L., Mayo, A. W., Louden, T., et al. 2018, *AJ*, 155, 107
- Mandel, K., & Agol, E. 2002, *ApJL*, 580, L171
- Millholland, S., & Laughlin, G. 2017, *AJ*, 154, 83
- Morris, S. L. 1985, *ApJ*, 295, 143
- Mo nik, T., Hellier, C., Anderson, D. R., Clark, B. J. M., & Southworth, J. 2017, *MNRAS*, 469, 1622
- Mo nik, T., Hellier, C., & Southworth, J. 2018, arXiv:1804.05334
- Newville, M., Stensitzki, T., Allen, D. B., et al. 2016, *Astrophysics Source Code Library*, ascl:1606.014
- Parmentier, V., & Crossfield, I. J. M. 2018, *Handbook of Exoplanets*, 116
- Peale, S. J., Cassen, P., & Reynolds, R. T. 1979, *Lunar and Planetary Science Conference*, 10, 964
- Pfahl, E., Arras, P., & Paxton, B. 2008, *ApJ*, 679, 783
- Placek, B., Knuth, K. H., & Angerhausen, D. 2016, *PASP*, 128, 074503

- Quintana, E. V., Rowe, J. F., Barclay, T., et al. 2013, *ApJ*, 767, 137
- Rabus, M., Jordán, A., Hartman, J. D., et al. 2016, *AJ*, 152, 88
- Rauer, H., Catala, C., Aerts, C., et al. 2014, *Experimental Astronomy*, 38, 249
- Ricker, G. R., Winn, J. N., Vanderspek, R., et al. 2015, *Journal of Astronomical Telescopes, Instruments, and Systems*, 1, 014003
- Sanchis-Ojeda, R., Rappaport, S., Pallè, E., et al. 2015, *ApJ*, 812, 112
- Sanchis-Ojeda, R., Rappaport, S., Winn, J. N., et al. 2013, *ApJ*, 774, 54
- Serrano, L. M., Barros, S. C. C., Oshagh, M., et al. 2018, *A&A*, 611, A8
- Sing, D. K., Fortney, J. J., Nikolov, N., et al. 2016, *Nature*, 529, 59
- Shporer, A. 2017, *PASP*, 129, 072001
- Shporer, A., & Hu, R. 2015, *AJ*, 150, 112
- Shporer, A., O'Rourke, J. G., Knutson, H. A., et al. 2014, *ApJ*, 788, 92
- Shporer, A., Wong, I., Huang, C. X., et al. 2018, arXiv:1811.06020
- Sinukoff, E., Howard, A. W., Petigura, E. A., et al. 2017, *AJ*, 153, 271
- Smith, A. M. S., Anderson, D. R., Armstrong, D. J., et al. 2014, *A&A*, 570, A64
- Smith, A. M. S., Cabrera, J., Csizmadia, S., et al. 2018, *MNRAS*, 474, 5523
- Tinetti, G., Drossart, P., Eccleston, P., et al. 2016, *Proc. SPIE*, 9904, 99041X
- Van Cleve, J. E., Howell, S. B., Smith, J. C., et al. 2016, *PASP*, 128, 075002
- Vanderburg, A., & Johnson, J. A. 2014, *PASP*, 126, 948
- Vanderburg, A., Latham, D. W., Buchhave, L. A., et al. 2016, *ApJS*, 222, 14
- VanderPlas, J. T., & Ivezić, Ž. 2015, *ApJ*, 812, 18
- White, T. R., Pope, B. J. S., Antoci, V., et al. 2017, *MNRAS*, 471, 2882
- Winn, J. N. 2010, arXiv:1001.2010